Bubble Generation Rules in Microfluidic Devices with Microsieve Array as Dispersion Medium

Chen Zheng, Bochao Zhao, Kai Wang, and Guangsheng Luo
The State Key Laboratory of Chemical Engineering, Dept. of Chemical Engineering, Tsinghua University, Beijing 100084, China

DOI 10.1002/aic.14765
Published online March 2, 2015 in Wiley Online Library (wileyonlinelibrary.com)

Microfluidic devices with microsieve array as the dispersion medium have been well recognized. However, few studies have been made on gas-liquid two-phase flow in microsieve dispersion devices. The bubble generation rules with single-pore, radial-array pores, axial-array pores, and square-array pores were systematically investigated. The rules of pore activation have been suggested by considering the capillary force, flow resistances of both dispersed phase and continuous phase. An empirical equation and a theoretical equation to predict the activation of pores in microfluidic devices were developed. An equation to correlate the average bubble diameter with parameter of channel structure, phase ratio, and Ca number of continuous phase was also developed. The strategy of design and scaling up for microsieve devices is proposed. Meanwhile, a device with dual-size pores according to the rules derived is designed. This device achieved much better dispersion performance. © 2015 American Institute of Chemical Engineers *AIChE J*, 61: 1663–1676, 2015
Keywords: multiphase flow, bubble generation rules, microsieve device, scale-up

Introduction

Gas-liquid dispersion processes can be found in many fields,[1–4] such as flotation, distillation, absorption purification of gas, and chemical reactions fermentation, and food processing. The interfacial area determined by bubble size is one of the key parameters in these gas-liquid processes. Larger area could lead to a better transfer and reaction performances.[5–7] So, the controllable generation of bubbles are highly required.

During recent years, microfluidic devices have been used in emulsification, material synthesis, biochemistry, gas purification, and chemical reaction processes for their high efficiency, controllability, and safety.[8–10] Monodispersed and micrometer-scaled bubbles and droplets can be controllably prepared in microfluidic devices based on cross-flowing,[11] coflowing,[12] and hydrodynamic flow-focusing.[13] The generation rules of droplets and bubbles in microfluidic devices with single dispersion element have been studied by experiments or by numerical simulation.[14] All the microfluidic devices could be well applied in small scale processes, but not suitable to large scale applications very well. A feasible way to scale up the microdevices is highly required. Accordingly, the devices with microchannel array,[15] microjunction array,[16] and microsieve plate[17] were developed. Among them, microsieve dispersion device is widely used for its simpler structure and variability. In our previous work, such device has been used for controllable preparation of nanoparticle.[18] Wang et al.[19] proposed the droplet generation rules in microsieve dispersion device. It was found that the *Ca* number of continuous phase and channel size mainly influence the droplet size. The mass transfer of liquid-liquid system in such devices was studied by Shao et al.[20] However, we still need more studies on bubble generation rules in microsieve dispersion devices for gas-liquid system.

There are many differences between liquid-liquid and gas-liquid system. First, the interfacial tension between gas and liquid phases is usually much higher than that between liquid and liquid phases. Thus, interfacial tension caused pressure and the capillary pressure are relatively higher in gas-liquid systems. Second, the viscosity of gas is usually much lower than that of liquid. Thus, the flow resistance in pores caused pressure is relatively lower in gas-liquid systems. As a result, the interfacial tension caused pressure and the capillary pressure may lead the main effects on the activation of pores. The generation rules of bubbles are different from that of droplets. Therefore, the bubble generation rules in microsieve dispersion devices have been studied in this work. Twelve microfluidic devices with special pore arrays have been designed. The effects of channel structure, pore arrangement, and flow rate on the average size and distribution of bubbles have been investigated. A model considering all the parameters mentioned above to predict the average size of bubbles has been developed. Some general rules for reliable design and application of microsieve dispersion devices to gas-liquid processes are discussed.

Experimental

Materials

We used 1 wt % sodium dodecyl sulfate (SDS) and 5 wt % polyethylene glycol (PEG) aqueous solution as the continuous phase. SDS was used as surfactant. We measured the

Correspondence concerning this article should be addressed to G. S. Luo at gsluo@tsinghua.edu.cn.

Table 1. Surface Tension and Viscosity of the Continuous Phases

	γ (mN/m) (26 °C)	μ (mPa s) (26 °C)
1% SDS + 5% PEG	34.23	1.83
1% SDS	27.15	1.00

viscosities by a viscometers (LVDV) purchased from Brookfield Engineering Laboratories and surface tensions by an optical contact-measuring device (series OCA) purchased from Dataphysics Instruments GmbH. The fluid with 1 wt % SDS was used in D1–D3 microfluidic devices while the fluid with 1 wt % SDS and 5 wt % PEG 4000 was used in the other devices. The PEG was used to increase the *Ca* number while maintaining a suitable flow rate of the continuous phase. The physical properties of the continuous phases are listed in Table 1. PEG with a molecular weight of 4000 was purchased from Beijing Modern Oriental Fine Chemistry Co. Nitrogen (N_2) at 99.995 mol % was purchased from Beijing Huayuan Gas Chemical Industry Co. Analytically pure SDS was purchased from Beijing Modern Oriental Fine Chemistry Co.

Experimental setup

The experimental setup shown in Figure 1 consists of three parts: transportation, microdevice, and observation part. The nitrogen was delivered through a mass flow meter with a measurement accuracy of ±1.0%. Liquid phase was transported in an indirect way. The solution was stored in a piston buffer tank. An advection pump with a measurement accuracy of ±1.0% was used to pump the water into the tank to push the piston. Then, the piston pushed the solution into the contactor. Before the experiment, we would make sure that no air exists in the tank. A water bath with a resolution of ± 0.1 K was used to maintain the experimental temperature. All the 12 devices shown in Figure 2 are divided into four groups: single-pore, radial-array pores, axial-array pores, and square-array pores devices. The structural parameters of the microsieve devices are listed in Table 2. In D1–D11 devices, the pore diameter is 0.31 mm. In D12 device, the diameter of upstream pore is 0.31 mm while the diameter of downstream pore is 0.27 mm. The gas phase was dispersed into the liquid phase through the pore-array chips made of polymethyl methacrylate (PMMA). The microfluidic chips were sealed with other two PMMA plates by a thermocompressor purchased from ShenZhen Techson Technology Co.[19] The chip was placed on the top of the main channel attached with an observation room at the exit. Inlet chamber and inlet channel were placed on the top of the chip. A pressure gage with a measurement accuracy of ±1% was installed at the entrance of device to measure the pressure drop through the microdevice. We pumped the continuous phase into the devices for 2 h before the dispersed phase was introduced into the devices, considering the effect of surfactant on the wetting property of channel walls. To ensure a stable condition, the flow was maintained for 2 min prior to every measurement.

Operation and analysis

We used a CCD camera to observe the flow in the main channel and observation room. Images and videos were recorded at a constant frequency of 2000 frames/s. From the images, we could analyze the distribution of bubbles by measuring the diameter of every bubble directly. The polydispersity index (PDI) was used to represent the uniformity of bubble sizes. It is defined as following equation

$$\sigma = \delta^* / d_{av}{}^* \times 100\% \tag{1}$$

δ^* represents the standard deviation of the apparent bubble diameter, and $d_{av}{}^*$ represents the average bubble size of at least 100 bubbles. Monodispersed bubbles are only achieved when the PDI is less than 5%. We could also calculate the average bubble size by the following equation

$$d_{av} = \sqrt[3]{6Q_d/\pi f} \tag{2}$$

Q_d represents the volume flow rate of dispersed phase, and f represents the generation frequency of bubbles. This equation is used when the shape of bubbles observed in images is irregular. In each experiment, we could make sure that no coalescence occurred.

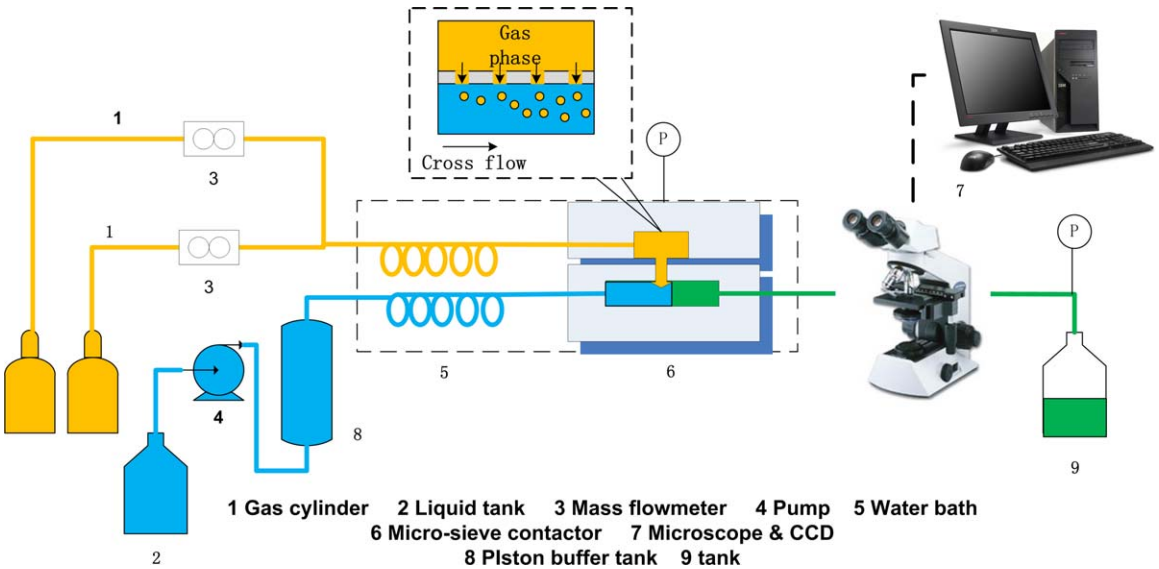

Figure 1. Experimental setup.

[Color figure can be viewed in the online issue, which is available at wileyonlinelibrary.com.]

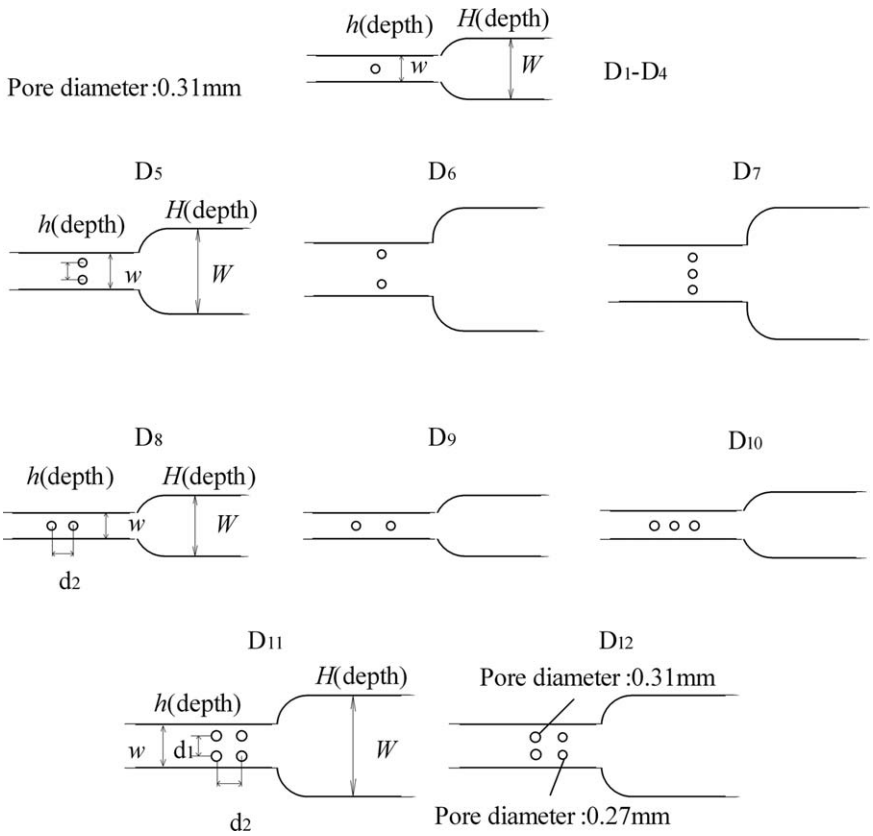

Figure 2. The schematic diagrams of microsieve dispersion devices in the experiment.

D_1–D_4, single pore; D_5–D_7, radial-array pores; D_8–D_{10}, axial-array pores; D_{11}–D_{12}, square-array pores.

Results and Discussion

In this work, the gas phase was injected from the side channel into the stream of liquid, hence the generation rule is similar to that in T-junctions. All experimental conditions are mainly in the transition region from bubbly flow to slug flow. In this region, numerous bubbles were observable as the gas was dispersed in the form of discrete bubbles in the continuous liquid phase.

Bubble generation in single-pore microdevices

Bubbles were ruptured regularly in microdevices D_1, D_2, D_3, and D_4, just as in typical T-junction microfluidic devices. The average diameters of bubbles are shown in Figure 3. The average bubble size decreases with the increase of the flow rate of the continuous phase (*Ca* number). The bubble size increases as the channel widens. The average diameter of bubbles changes from 2000 to 550 μm while the *Ca* of the continuous phase ($Ca_c = \frac{\mu_c u_c}{\gamma}$) ranges from 0.0005 to 0.012. It is found that the flow rate of the dispersed phase also has effect on the bubble size. To investigate the effect of flow rate of the dispersed phase on bubble generation further, we increased the flow rate of the dispersed phase in device D_4. To increase the Ca_c while maintaining a suitable flow rate of the continuous phase, we used 1 wt % SDS and 5 wt % PEG 4000 aqueous solution as the continuous phase. From Figure 3, we can find that the average bubble size increases as the flow rate of the dispersed phase increases, the flow pattern changes from bubbly flow to slug flow as the ratio of flow rates of the dispersed and continuous phase increases.

From the experimental results, we built a quantitative model considering the channel size, the flow rates of the two phases to predict the bubble size. However, this model does not contain parameters of the pore size and shape, all pore sizes are uniform. The bubble size is determined by the coeffect of interfacial tension and shearing force (represented by the Ca_c) and Q_d/Q_c. It can be expressed by following equation

$$d_{av}/d_e = \alpha\left(\frac{Q_d}{Q_c}\right)^{\beta 1} Ca^{\beta 2} \tag{3}$$

d_{av} represents the average diameter of bubbles, d_e represents the hydraulic diameter of the main channel ($d_e = 2wh/(w+h)$). Along with surface tension and viscosity, compressibility is also a distinct property of a gas when compared with liquids. We measured the pressure of the gaseous disperse phase through a pressure gage with a measurement

Table 2. The 3-D Structural Parameters of Microsieve Devices

	w (mm)	h (mm)	W (mm)	H (mm)	d_1 (mm)	d_2 (mm)	d_p (mm)
D_1	0.60	0.60	2.0	1.0			0.31
D_2	0.90	0.60	2.5	1.0			0.31
D_3	1.50	0.60	3.0	1.0			0.31
D_4	2.00	0.60	3.0	1.0			0.31
D_5	1.75	0.60	3.0	1.0	1.0		0.31
D_6	3.00	0.60	4.0	1.0	1.5		0.31
D_7	3.00	0.60	4.0	1.0	1.0		0.31
D_8	1.20	0.60	2.0	1.0		1.0	0.31
D_9	1.20	0.60	2.0	1.0		2.0	0.31
D_{10}	1.20	0.60	2.0	1.0		1.0	0.31
D_{11}	2.00	0.60	3.0	1.0	1.0	2.0	0.31
D_{12}	2.00	0.60	3.0	1.0	1.0	2.0	0.31/0.27

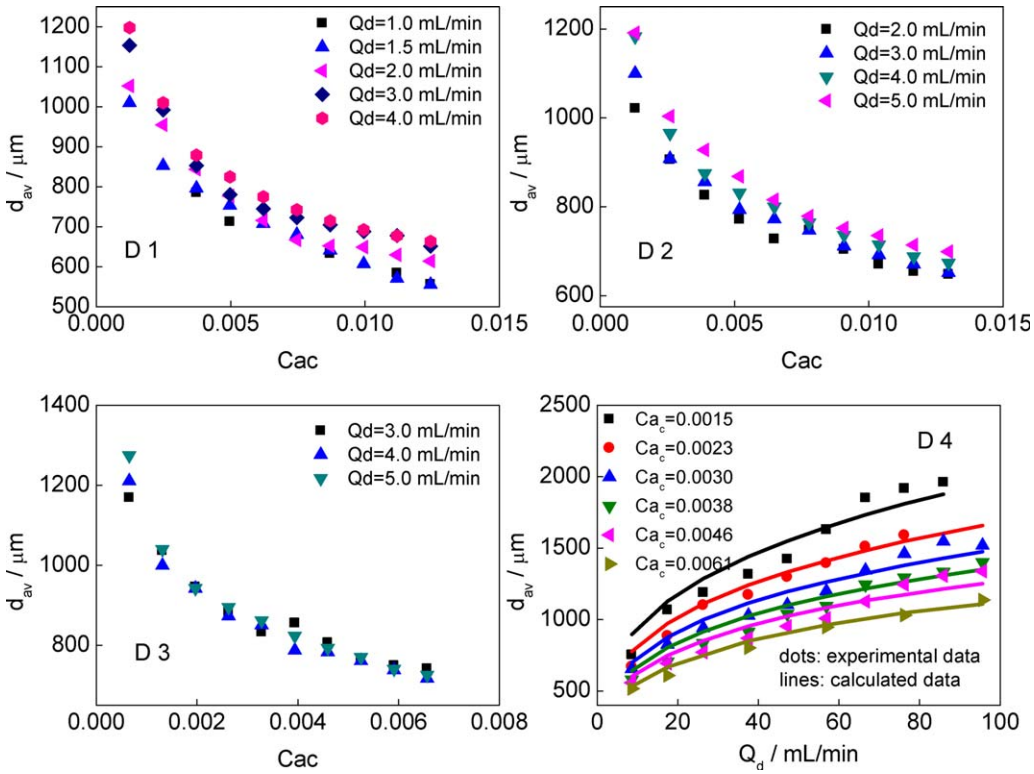

Figure 3. The average diameters of bubbles in single-pore devices.

(D_1: $w = 0.6$ mm, $h = 0.6$ mm; D_2: $w = 0.9$ mm, $h = 0.6$ mm; D_3: $w = 1.5$ mm, $h = 0.6$ mm; D_4: $w = 2.0$ mm, $h = 0.6$ mm). [Color figure can be viewed in the online issue, which is available at wileyonlinelibrary.com.]

accuracy of ±0.1 kPa. The pressures in our experiment ranged from 3 to 40 kPa. We took the difference of pressure into consideration while we revised the Q_d. Using nonlinear fitting, we can get the values of parameters in Eq. 3, as shown in Table 3. The dimensionless average bubble diameter has a linear relation with $(\frac{Q_d}{Q_c})^{0.33}$, which is close to the conclusion of previous work.[21] Using the model, we could calculate the bubble diameter in different conditions, the calculated data fit the experimental data well, as shown in Figure 4. However, for D_4 device, at higher gas flow rate and lower continuous phase flow rate, the predicted results do not match the experimental result well due to the changing of flow pattern to slug flow.

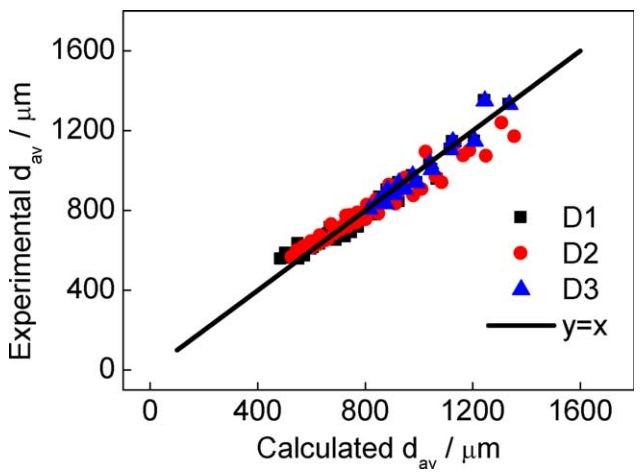

Figure 4. Comparison between calculated data and experimental data in single-pore devices.

[Color figure can be viewed in the online issue, which is available at wileyonlinelibrary.com.]

Bubble generation in microfluidic devices with radial-array pores

It can be observed that the dispersed phase does not pass through all pores in the microsieve array microdevices at some experimental conditions. We define that the pores with the dispersed phase passing through are active pores. The distribution of active pores in the microdevices with radial-array pores is shown in Figure 5. As the flow rate of the dispersed phase increases at a constant flow rate of the continuous phase, the number of active pores increases from 1 to 3. The pores also seem easier to be activated when the flow rate of the continuous phase is higher, as a higher flow rate can lead to a smaller bubble size, which reduces the steric hindrance. We discuss the transition of active-pore number from 1 to 2 (or 2 to 3). A schematic of the pressure drop through pores is shown as Figure 6.

The pressure drop in an active pore caused by flow resistance of the dispersed phase, including the Hagen–Poiseuille's resistance ($R_{HP} = \frac{128 l_p}{\pi d_p^4}$) and Sampson's resistance ($R_S = \frac{24}{d_p^3}$) can be calculated by the following equation[18,22]

$$\Delta p_f = (R_{HP} + R_S)\mu_d u_d \frac{\pi d_p^2}{4} = \left(\frac{32 l_p}{d_p^2} + \frac{6\pi}{d_p}\right)\mu_d u_d \qquad (4)$$

Table 3. The Values of Parameters

	Fitted Value	Confidence Interval
α	1.18	1.12–1.24
$\beta 1$	0.33	0.32–0.34
$\beta 2$	−0.02	−0.03 to −0.01

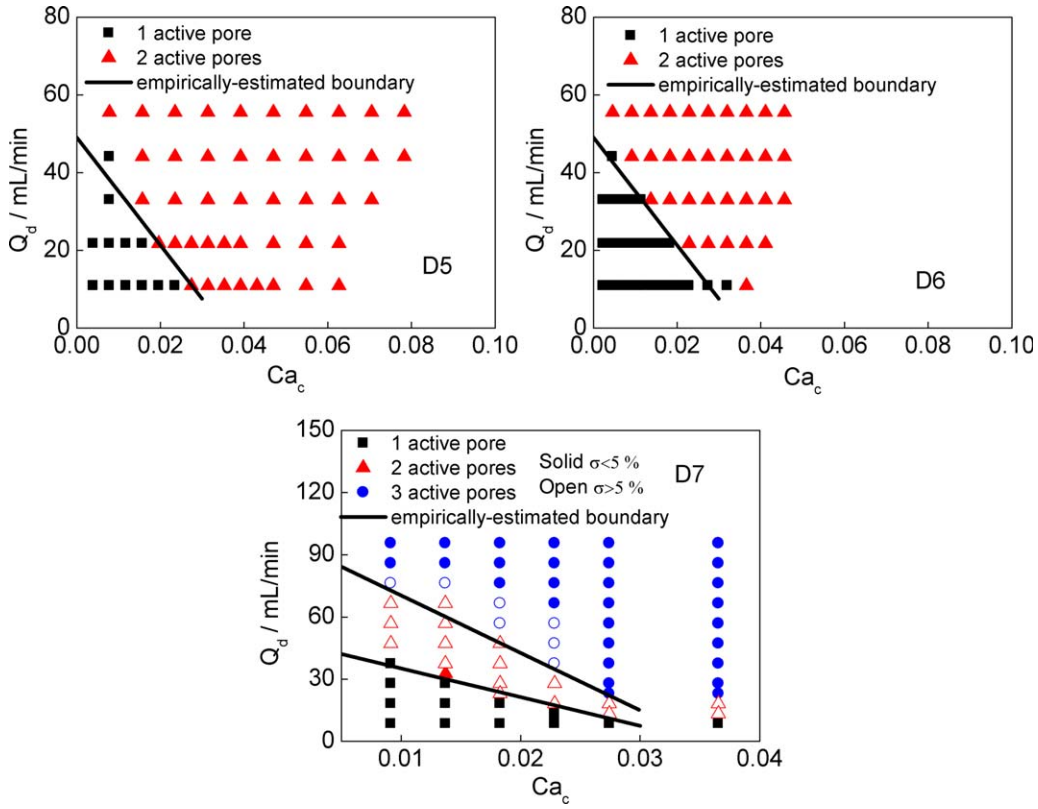

Figure 5. The distribution of active pores in microdevices with radial-array pores.

[Color figure can be viewed in the online issue, which is available at wileyonlinelibrary.com.]

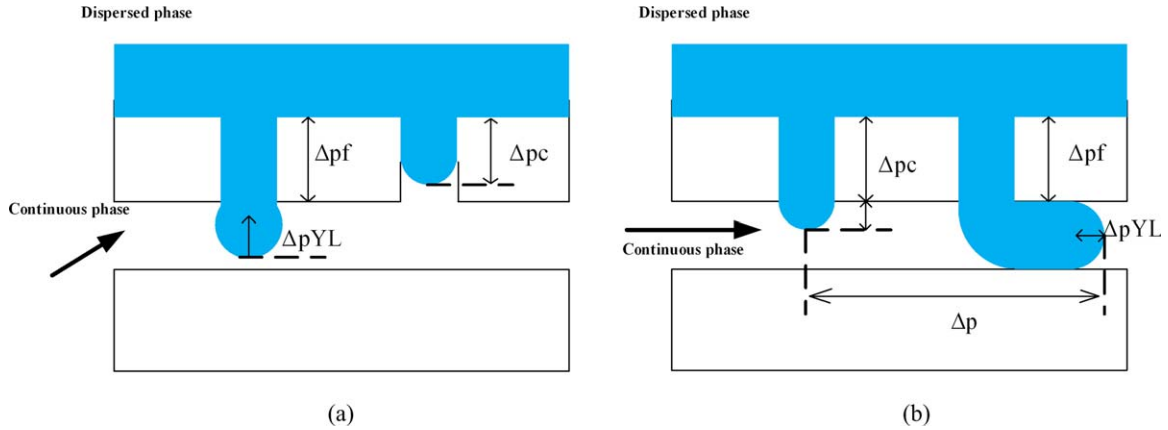

Figure 6. (a) Schematic of the pressure drop through radial-array pores; (b) schematic of the pressure drop through axial-array pores.

[Color figure can be viewed in the online issue, which is available at wileyonlinelibrary.com.]

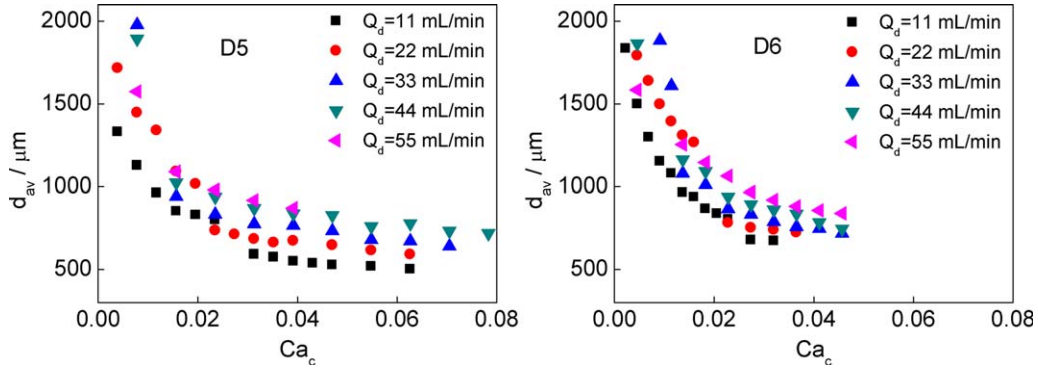

Figure 7. The average bubble sizes in microdevices with radial-array pores.

[Color figure can be viewed in the online issue, which is available at wileyonlinelibrary.com.]

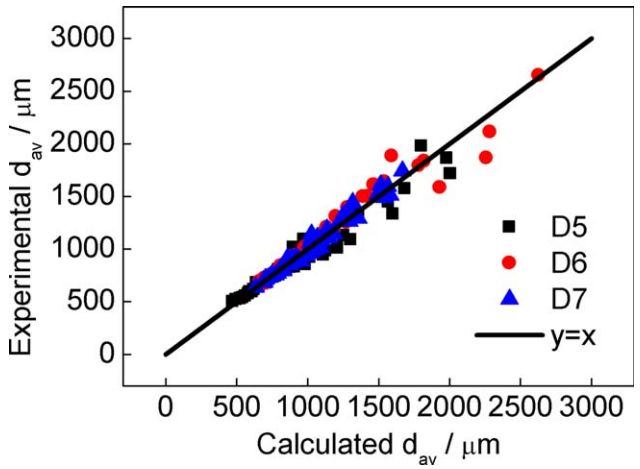

Figure 8. Comparison between calculated data and experimental data in D5–D7 devices with radial-array pores.

[Color figure can be viewed in the online issue, which is available at wileyonlinelibrary.com.]

where l_p represents the depth of pores, d_p represents the pore diameter, μ_d represents the viscosity of the dispersed phase, u_d represents the transpore flow velocity of dispersed phase.

The interfacial tension-induced pressure drop can be expressed by the Young–Laplace equation

$$\Delta p_{YL} = \frac{4\gamma}{d_b} \tag{5}$$

where γ represents the gas-liquid interfacial tension, d_b represents the bubble diameter.

The capillary pressure drop in pores can be expressed by the Young–Laplace equation

$$\Delta p_c = \frac{4\gamma\cos\theta}{d_p} \tag{6}$$

where $\cos\theta$ is taken as 1 for the straight edge of the pore. d_p represents the diameter of pore. The flow resistance-induced pressure drop of continuous phase can be expressed by the following equation

$$\Delta p = \lambda\frac{l}{d_e}\frac{\rho u_c^2}{2} = 31\frac{\mu_c l}{d_e^2}u_c \tag{7}$$

The interfacial tension-induced pressure drop of pore 2 decreases with bubble growth. At the beginning and the end of bubble generation

$$\begin{cases} t = 0, d = d_p, \Delta p_{YL2} = \Delta p_{YL2,max} \\ t = t_s, d = d_b, \Delta p_{YL2} = \Delta p_{YL2,min} \end{cases} \tag{8}$$

where t_s represents the time of bubble generation. The pressure balance between the two adjacent pores 1 and 2 is shown in Eq. 9

$$\Delta p_{f1} = \left(\frac{32 l_p}{d_p^2} + \frac{6\pi}{d_p}\right)\mu_d u_{d1} = \Delta p_{f2} + \Delta p_{YL2} - \Delta p_{YL1} - \Delta p \tag{9}$$

u_{d1} can be calculated by Eq. 9, the criterion of activation is $\int_0^{t_s} u_{d1}dt = 0$. When $\int_0^{t_s} u_{d1}dt > 0$, the total flow rate of the dispersed phase through pore 1 is positive during the period of bubble generation in through pore 2, hence the pore 1 can be activated in exact. When $\int_0^{t_s} u_{d1}dt < 0$, the total flow rate of the dispersed phase through pore 1 is negative, the pore 1

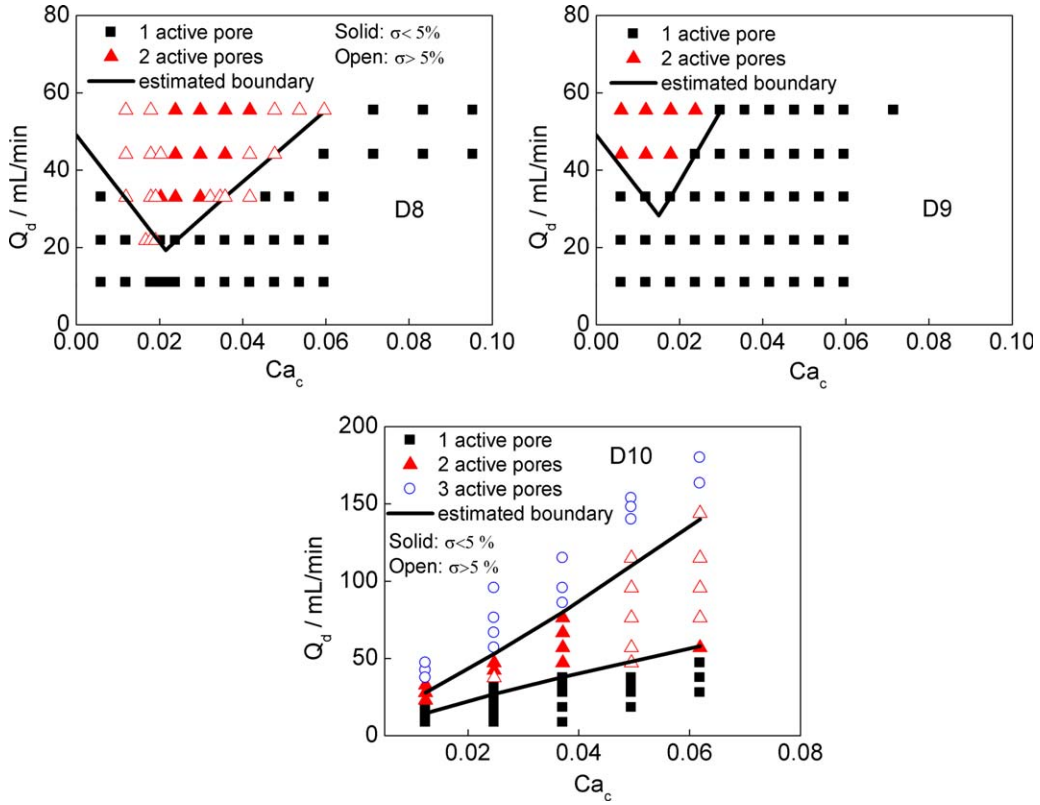

Figure 9. The distribution of active pores in microdevices with axial-array pores.

[Color figure can be viewed in the online issue, which is available at wileyonlinelibrary.com.]

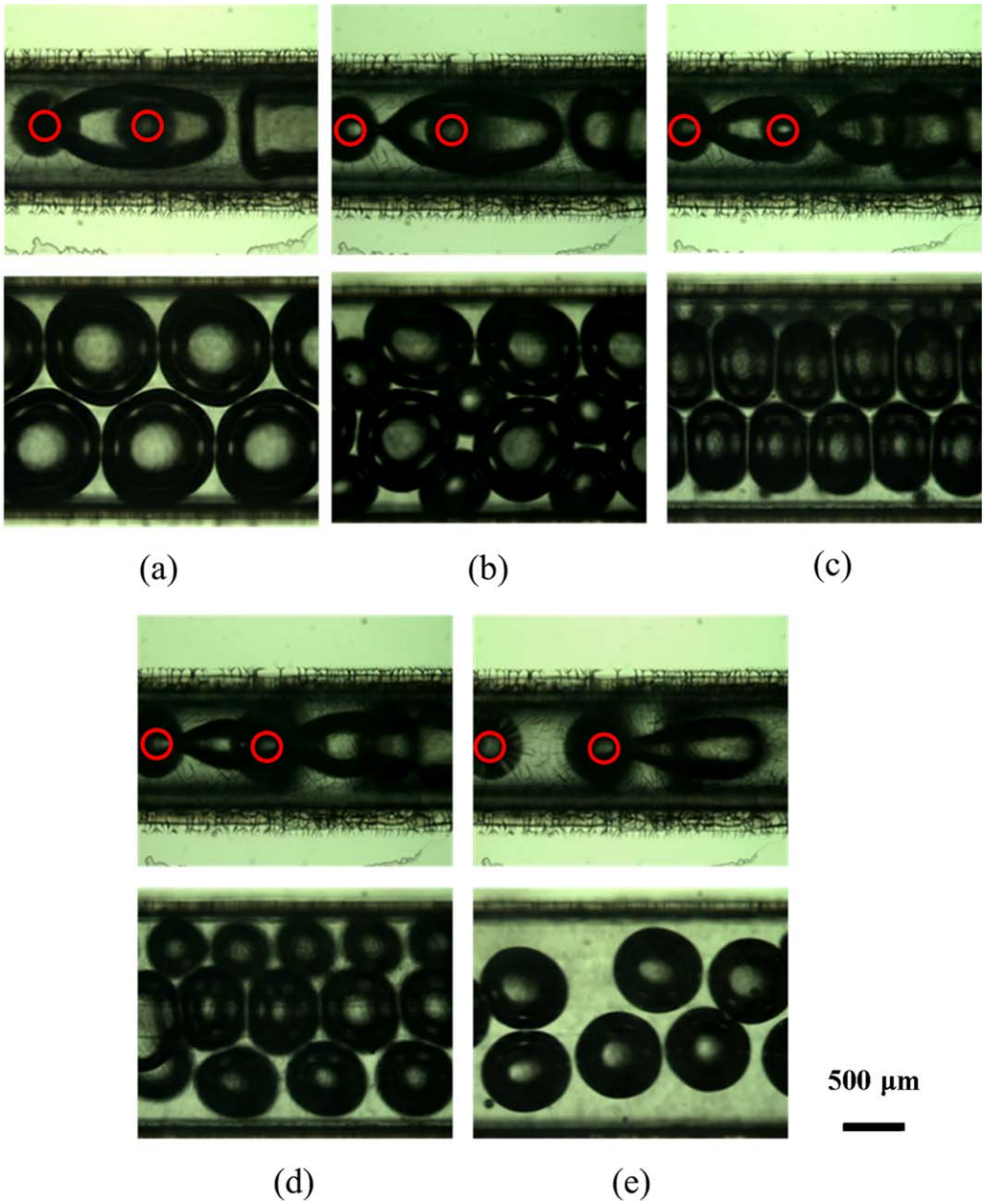

Figure 10. Bubble generation in D8 device with axial-array pores.

(The pore is specified by red circle, observed by the microscope from top to bottom. For each group of pictures, the upper one is the picture of dispersion channel while the lower one is the picture of observation channel.) (a) $Q_d = 33$ mL/min, $Q_c = 10$ mL/min; (b) $Q_d = 33$ mL/min, $Q_c = 16$ mL/min; (c) $Q_d = 33$ mL/min, $Q_c = 20$ mL/min; (d) $Q_d = 33$ mL/min, $Q_c = 30$ mL/min; (e) $Q_d = 33$ mL/min, $Q_c = 50$ mL/min. [Color figure can be viewed in the online issue, which is available at wileyonlinelibrary.com.]

remains inactive. It is difficult to find the analytical solution of the criterion. Thus, we use Ca_d ($Ca_d = \frac{\mu_d u_d}{\gamma}$) and Ca_c to empirically determine the criterion of activation.

We find that devices D5 and D6 have identical activation boundaries. Fitting the data on the boundaries gives a dimensionless Eq. 10. This fitted boundary is plotted in Figure 5

$$Ca_d = \frac{\mu_d Q_d}{\gamma A} = 0.0057 - 0.16\, Ca_c \tag{10}$$

where A represents the total active-pore area. We can use this criterion to predict the activation boundary between two and three active-pore regions, considering the difference of A. The predicted boundaries in device D7 are shown in Figure 5, which fit the experimental data well. We can determine the critical Ca_c for certain active-pore number at a given Q_d. When the flow rate of the continuous phase is smaller than critical Ca_c at the same dispersed phase flow rate, some pores will remain inactive.

The average bubble sizes are shown in Figure 7. The average bubble size strongly depends on the number of active pores. As the number of active pores changes, there is a significant change of the average bubble size. Comparing device D5 with device D6, we find that the bubble sizes between the two different channels are similar at the same gas flow rate and Ca number, except for the transition region of pore number. Hence, the distance between the pores has little effect on the activation of pores or the bubble size, when the distance is bigger than bubble size. When both

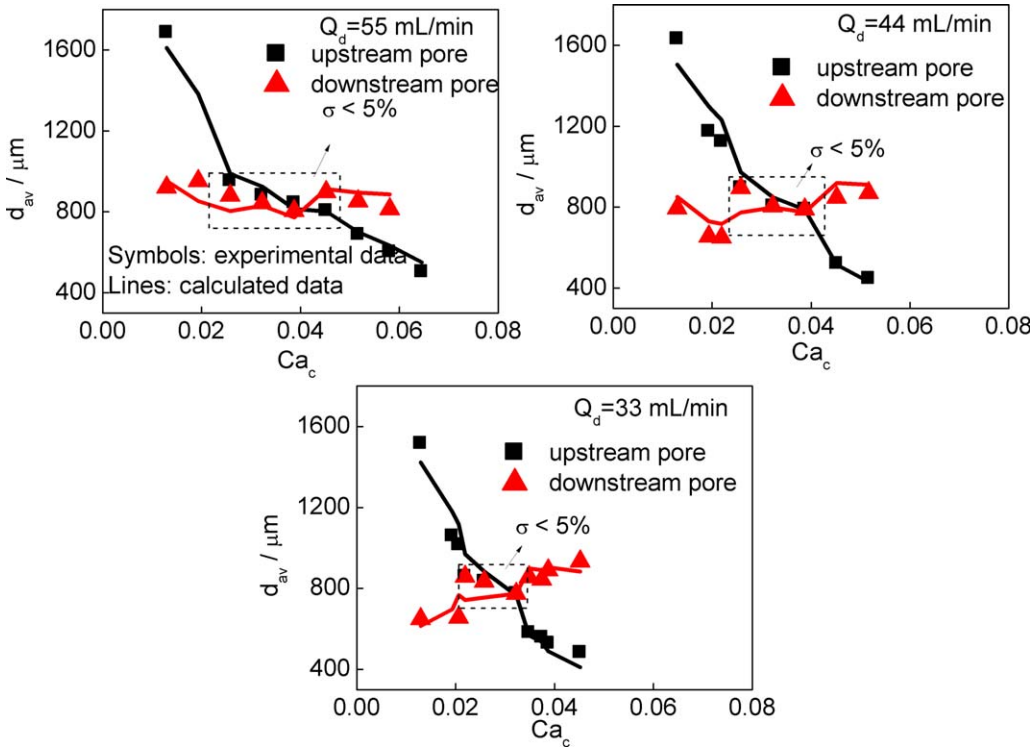

Figure 11. The average diameter of bubbles generated from upstream and downstream pores in devices with axial-array pores.

[Color figure can be viewed in the online issue, which is available at wileyonlinelibrary.com.]

pores are active, the frequency of bubble generation from each pore is the same. The gas volume is distributed equally into both pores in experimental conditions. However, the gas phase is not well-distributed in device D7 in some conditions, especially conditions with two active pores. The pore in the middle is different from the other two, which are hindered by the channel wall. In the condition of two active pores, bubbles come out of pores randomly. If two bubbles come out of the two side pores simultaneously, the sizes of them are equal. If one bubble comes out of the middle pore, while another one comes out of a side pore, the former will be hindered by only one side, not like the latter hindered by both the middle bubble and the channel wall. As a result, the bubble comes out of the middle pore will be bigger than that from the side pore. In the condition of three active pores, bubbles from each pore are hindered by both sides and turned to be more uniform. The steric hindrance is reduced when the size of bubbles turns smaller. Hence, the uniformity is better at higher Ca_c, as shown in Figure 5.

The average diameter of bubbles can also be predicted by the model derived in single-pore devices. In the devices with multiple pores, the volume flow rate of the dispersed phase needs to be modified according to the number of active pores. We use Eq. 11 instead of Eq. 3 to calculate the bubble size. The calculated data fit the experimental data well, as shown in Figure 8

$$d_{\mathrm{av}}/d_e = 1.18\left(\frac{Q_{\mathrm{d}}}{MQ_{\mathrm{c}}}\right)^{0.33} Ca^{-0.02} \tag{11}$$

where M represents the number of active pores.

Bubble generation in microfluidic devices with axial-array pores

The number of active pores in microfluidic devices with axial-array pores is shown in Figure 9. As the flow rate of the dispersed phase increases at a constant flow rate of the continuous phase, the number of active pores increases from 1 to 3. However, the pores seem more difficult to be active when the flow rate of the continuous phase is higher, as the higher flow rate can lead to bigger pressure drop between upstream and downstream pores. Comparing device D8 with device D9, we can find that as the distance between the two pores increases, the activation of the upstream pore becomes more difficult. At lower gas flow rate, as the flow rate of the continuous phase increases, the number of active pores changes from 1 (random pore) to 2 and back to 1 (downstream pore), as shown in Figure 10. Rules of bubble generation in microfluidic devices with axial-array pores turn to be more complex than that in microdevices with radial-array pores. The activation boundaries can be specified into two categories based on Ca_c. The activation boundary is similar to that in the devices with radial-array pores at lower Ca_c. This is because at lower Ca_c, the difference of pressure between upstream and downstream pore is less significant. In this case, we can use the empirical criterion in Eq. 10 to predict the activation boundary (the left boundaries in devices D8 and D9).

Then, we discuss the activation boundary at higher Ca_c. When both upstream (1) and downstream (2) pores are activated, the pressure balance can be expressed by the following equation. p_g represents the pressure in the inlet chamber, which is large enough to maintain a constant p_g

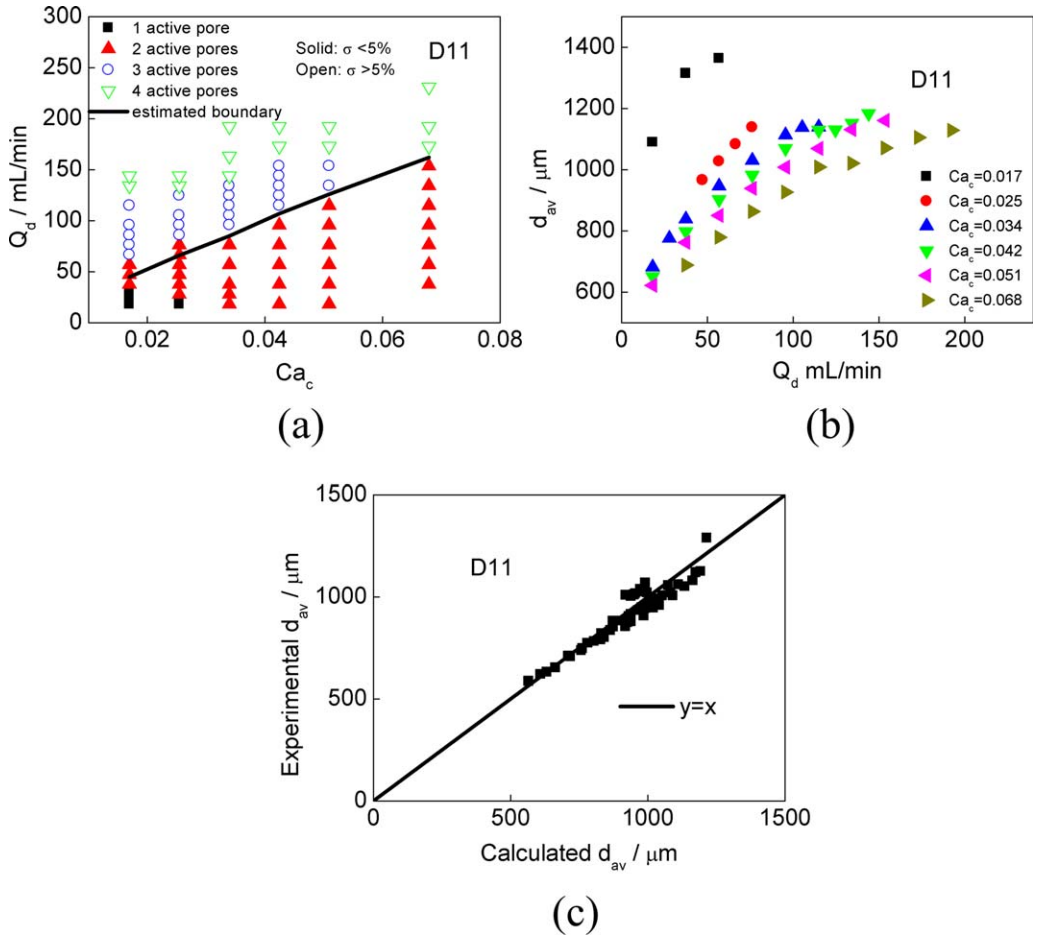

Figure 12. Experimental results of D11 device with uniform square-array pores.

(a) Distribution of active pores; (b) the average bubble diameters with PDI less than 5% in D11; (c) comparison between calculated data and experimental data. [Color figure can be viewed in the online issue, which is available at wileyonlinelibrary.com.]

$$\begin{aligned} p_g - \Delta p_{f1} - \Delta p_{\mathrm{YL1}} - \Delta p &= p_g - \Delta p_{f2} - \Delta p_{\mathrm{YL2}} \\ \Delta p_{f1} + \Delta p_{\mathrm{YL1}} + \Delta p &= \Delta p_{f2} + \Delta p_{\mathrm{YL2}} \end{aligned} \tag{12}$$

At higher continuous phase flow rate, a larger Δp will inhibit the activation of upstream pore. Upstream pore will not be active until the following equation is satisfied

$$\Delta p_{f1} + \Delta p_{\mathrm{YL1}} + \Delta p < \Delta p_{f2} + \Delta p_{\mathrm{YL2}} \tag{13}$$

Considering the extreme condition in which the gas phase is about to come out of the upstream pore, we can know that the flow rate through this pore is zero, as a result, $\Delta p_{f1} = 0$ and $\Delta p_{\mathrm{YL1}} = \Delta p_{\mathrm{c1}}$. As the maximum value of Δp_{YL2} is equal to the value of Δp_{c1}, ($\Delta p_{\mathrm{YL2_{max}}} = \frac{4\gamma}{d_{\mathrm{p}}} = \Delta p_{\mathrm{c1}}$) the criterion for upstream pore to be activated is $\Delta p < \Delta p_{f2}$. If $\Delta p > \Delta p_{f2}$, the upstream pore will not be active. Equation 14 is used to calculate the data on the boundary between regions of different number of active pores, as shown in Figure 8. The criterions of active-pore number transition fit the experiment data well. When the flow rate of the continuous phase is larger than that on the boundary at the same dispersed phase flow rate or the dispersed phase flow rate is smaller than that on the boundary at the same continuous phase flow rate, the upstream pore remain inactive

$$31\frac{l}{d_e^2}\mu_{\mathrm{c}}u_{\mathrm{c}} = \left(\frac{32l_{\mathrm{p}}}{d_{\mathrm{p}}^2} + \frac{6\pi}{d_{\mathrm{p}}}\right)\mu_{\mathrm{d}}u_{\mathrm{d}} \tag{14}$$

The bubble sizes were analyzed by the method of direct observation, while frequency of bubble generation from each pore along the channel was also recorded, so that we could calculate the flow rate of the dispersed phase through each pore. In device D8, when the flow rate of the continuous phase is relatively low, the gas phase comes out of the pore randomly. At a given flow rate of the dispersed phase, as the flow rate of the continuous phase increases, the PDI first decreases and then increases, as shown in Figure 11. The average diameter of bubbles from each single pore can also be predicted by the model. The volume flow rate of the dispersed phase needs to be considered independently. The calculated data fit the experimental data well, as shown in Figure 11.

Bubble generation in microfluidic devices with square-array pores

Microsieve device D11 with 2 × 2 microsieve pores was developed to test the distribution rule of bubbles. In this device, the pores are activated from downstream to upstream successively as the increase of flow rate of the dispersed phase at a given flow rate of the continuous phase, as shown in Figure 12a. First, a random downstream pore is activated

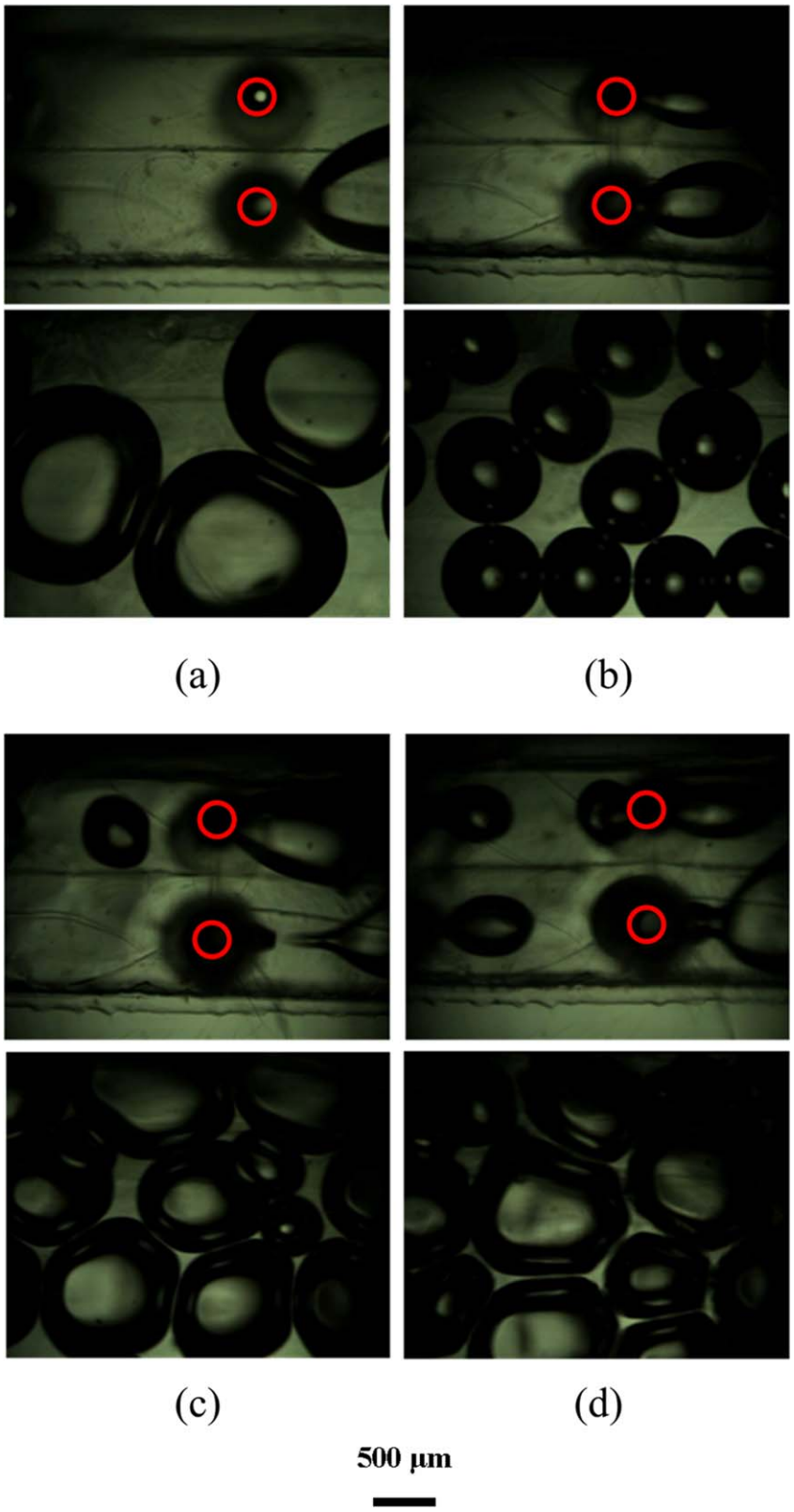

Figure 13. A diagram of bubble generation in D11 device.

(The pore is specified by red circle, observed by the microscope from top to bottom. For each group of pictures, the upper one is the picture of dispersion channel while the lower one is the picture of observation channel.) (a) One active pore with $Q_d = 30$ mL/min, $Q_c = 20$ mL/min; (b) two active pores with $Q_d = 30$ mL/min, $Q_c = 40$ mL/min; (c) three active pores with $Q_d = 110$ mL/min, $Q_c = 40$ mL/min; (d) four active pores with $Q_d = 170$ mL/min, $Q_c = 40$ mL/min. [Color figure can be viewed in the online issue, which is available at wileyonlinelibrary.com.]

at relatively low gas flow rate, then both downstream pores are activated. As the dispersed phase flow rate increases, a random upstream pore is activated, however, with significant low flow rate of the dispersed phase through it. The boundary between the regions of two and three active pores correlates well with the criterion proposed above, as shown in

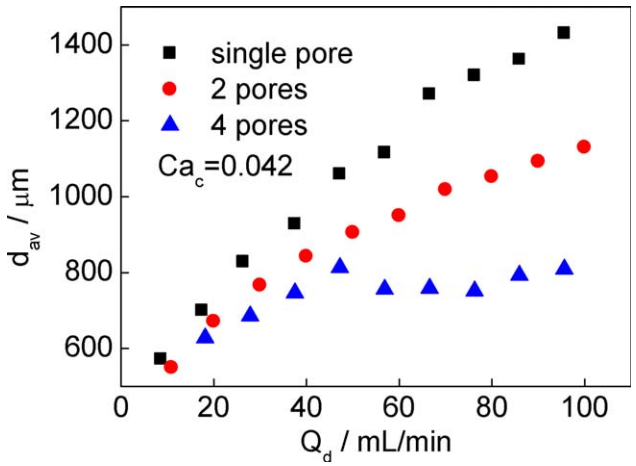

Figure 14. Comparison among three microsieve devices with different active pores.

[Color figure can be viewed in the online issue, which is available at wileyonlinelibrary.com.]

Figure 12a. All the pores are activated at relatively high gas flow rate. In this situation, the gas flow rates through the two upstream pores are same, the gas flow rates through the two downstream pores are also same. However, the gas flow rate through an upstream pore is much lower than that through a downstream pore due to the difference of pressure between the two pores. Monodispersed bubbles cannot be achieved in the condition with three or four active pores. Figure 13 shows the generation of bubbles from one active pore to four active pores. As the dispersed phase flow rate through the upstream pore is significantly lower than that through the downstream pore, increasing number of active pores has limited effect on the decreasing size of the bubbles. The average bubble diameters with PDI less than 5% are shown in Figure 12b. They fit the calculated data derived by the model well, as shown in Figure 12c.

Design and optimization for microsieve dispersion device

Deeper investigation on gas-liquid microdispersion device has been done in order to prepare uniform microbubbles in a large scale for industrial application. As the flow rate of the dispersed phase increases at a constant continuous phase flow rate, the performance of single-pore device on gas-liquid microdispersion is limited. The increase of active-pore number can lead to a significant decrease of bubble size, as shown in Figure 14. The three devices have different ratio of total active-pore area (with equal pore diameter) to the generation area. By introducing microsieve devices, we can get uniform microbubbles in smaller size.

The generation rules can guide the design of microsieve dispersion device under a given operating condition (Q_d and Q_c). First, we should keep the channel depth h in a scale of submillimeter in order to prepare microbubbles. Then, we can empirically choose a pore number according to the operating condition and required bubble size. When the active-pore number is determined, the d_e and Ca_c can be determined according to Eq. 11. As microfluidic devices with radial-array pores have wider operating range, we should consider them preferentially. However, two criteria should be satisfied, as shown in Eqs. 15 and 16

$$w \geq M d_{av} \tag{15}$$

$$\frac{\mu_d Q_d}{\gamma(M-1)a} \geq 0.0057 - 0.16\frac{\mu_c Q_c}{\gamma w h} \tag{16}$$

where a represents single pore area. Equation 15 shows the effect of distance between two adjacent pores. The distance

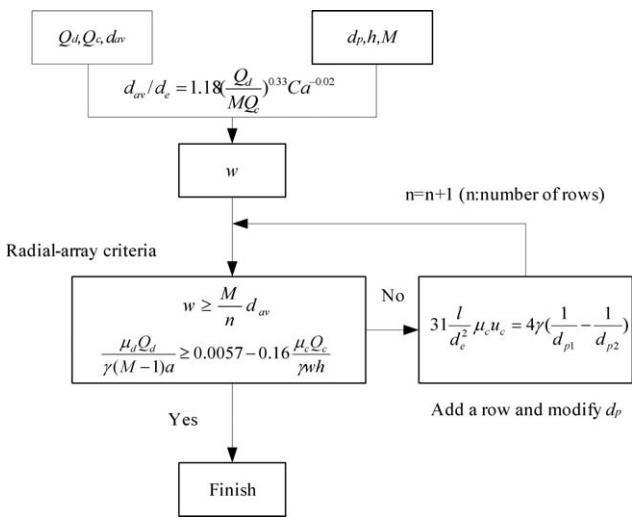

Figure 15. Design schematic of microsieve dispersion device.

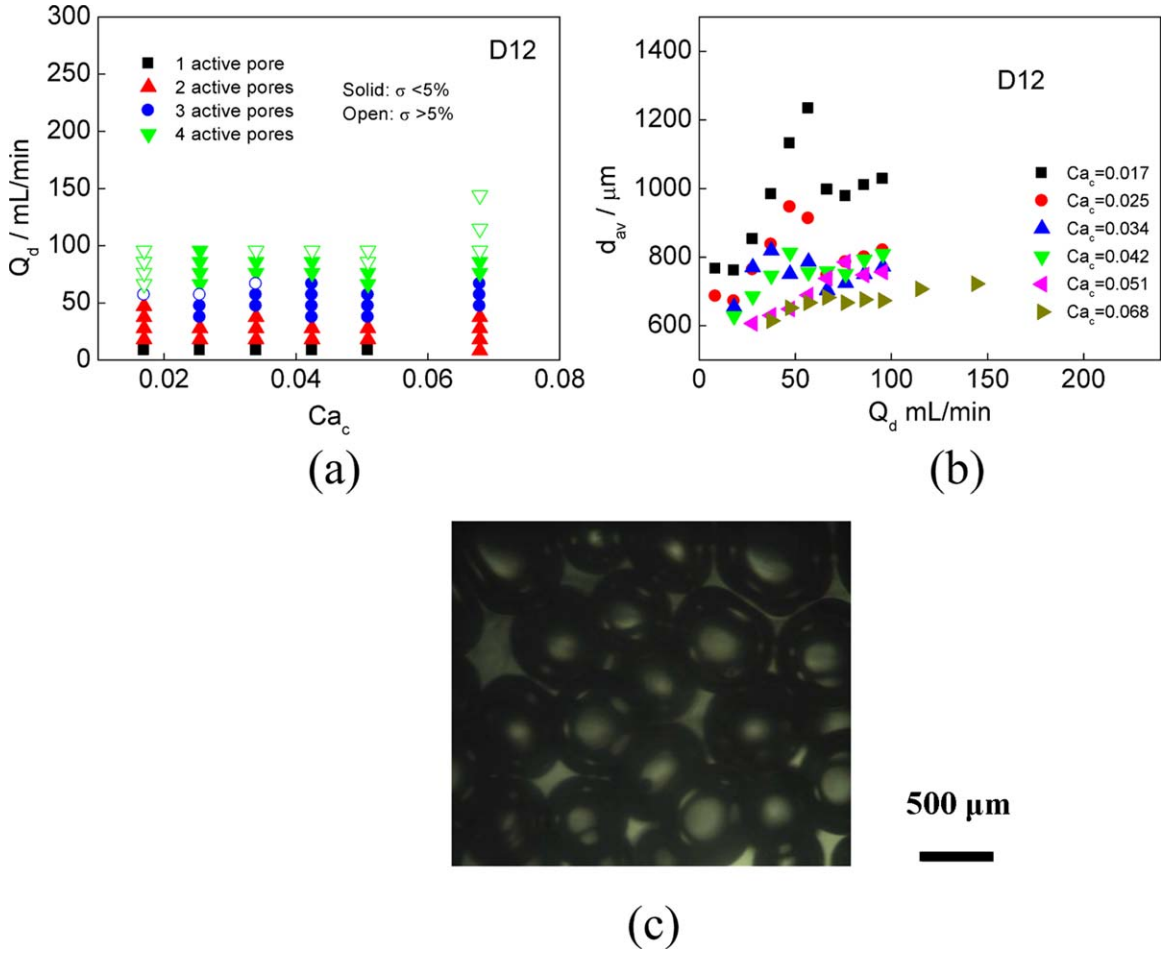

Figure 16. Experimental results of D12.

(a) Distribution of active pores; (b) the average bubble diameters; (c) diagram of D12 device with four active pores ($Q_d = 80$ mL/min, $Q_c = 40$ mL/min). [Color figure can be viewed in the online issue, which is available at wileyonlinelibrary.com.]

should be at least as long as the bubble diameter, otherwise some pores will be cut out. Equation 16 derived from Eq. 10 shows activation criterion of all the pores in microfluidic devices with radial-array pores. If these two criteria cannot be satisfied simultaneously, we need to change the arrangement of pores to square-array. For square-array device, we need to take the difference of pressure between upstream and downstream pores into consideration, mentioned in Bubble generation in microfluidic devices with square-array pores section. This difference may lead to a nonuniform distribution of dispersed phase flow rate. We can optimize the structure of microsieve device by modifying the pore size to balance the pressure difference. A schematic of the design is shown in Figure 15.

We designed a 2 × 2 microsieve device with dual-size pores following the generation rules. As the flow rate of the continuous phase changes from 10 to 80 mL/min in our experiment, the pressure drop between upstream and downstream pores ranges from 22.5 to 180 Pa. In this device, the diameter of upstream pore was designed as 310 μm while the diameter of downstream pore was 270 μm. The diameter difference results in a capillary pressure difference of 65.4 Pa and a transpore pressure drop difference, both of which can balance the pressure difference induced by the flow of continuous phase. The distribution of active pores in microfluidic device with radial-array pores is shown in Figure 16a. Moreover, the PDI of the bubble size in device D12 is smaller, as the pressure distribution within upstream and downstream pores is more balanced. The region with good uniformity in device D12 is wider than that in device D11, especially in the conditions with three or four active pores, as shown in Figure 16a.

The average bubble diameters are shown in Figure 16b. Because the flow is distributed evenly in each pore, the bubble diameter decreases significantly while the number of active pores increases. Equation 11 is used to calculate the diameter of bubbles, considering the number of active pores. The calculated data fit the experimental data well, as shown in Figure 17.

Conclusion

We investigated the rules of bubble generation in microsieve dispersion devices for a gas-liquid system. The activation of pore is mainly determined by capillary force, interfacial tension, flow resistance of both the dispersed phase and continuous phase. The gas-liquid dispersion characteristics in microsieve devices

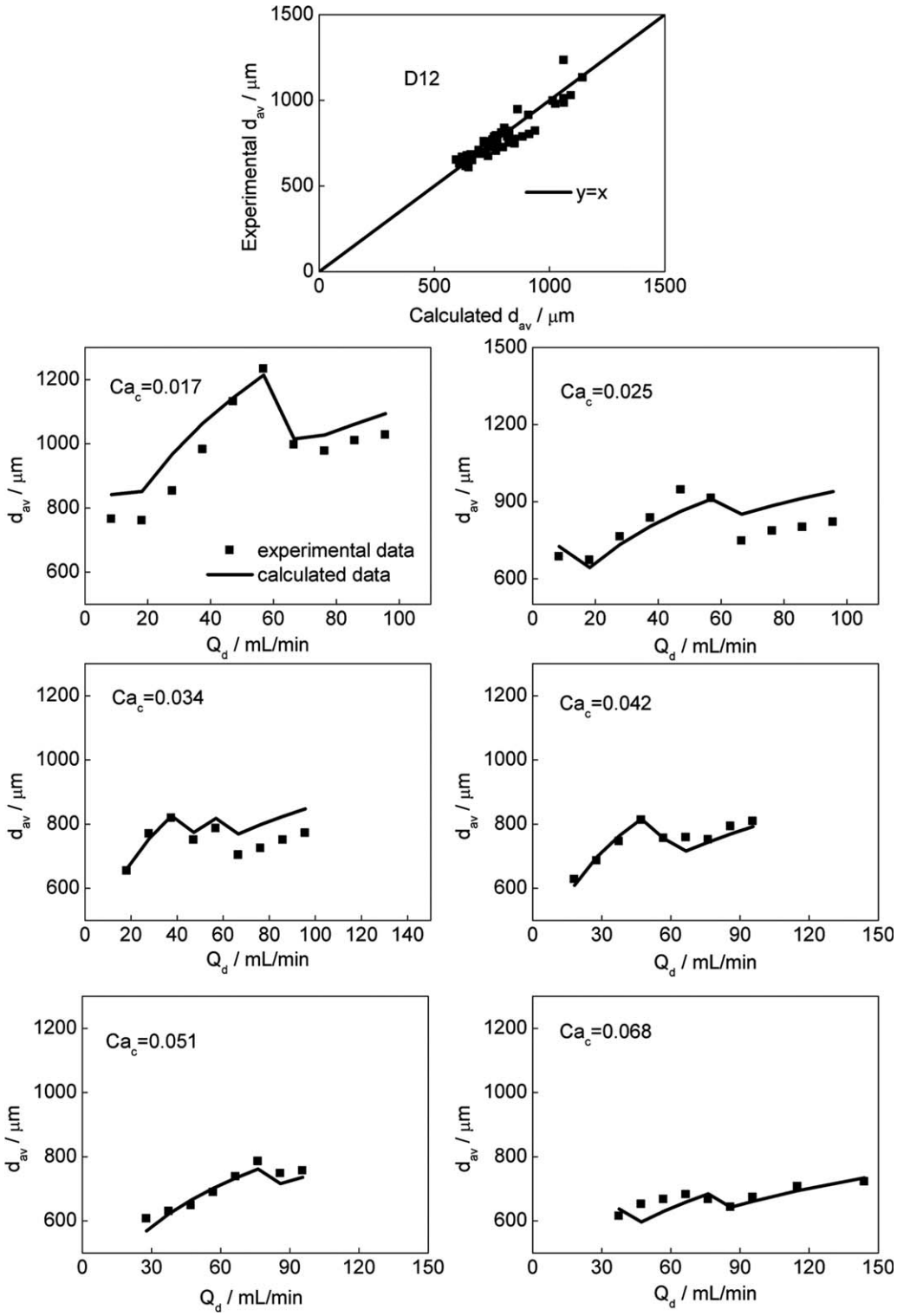

Figure 17. Comparison between calculated data and experimental data in D12.

are different from liquid-liquid dispersion. Compared with liquid-liquid systems, gas-liquid systems generally have a higher interfacial tension, thus capillary force and interfacial tension dominate the balance of force. Conversely, gas has much lower viscosity compared with liquid. As a result, the transpore resistance of the dispersed phase is much lower than that of the liquid-liquid system. In this case, the flow resistance of the continuous phase cannot be neglected. These two forces determine the activation of pores arranged as axial-array. We determined an activation boundary to predict the activation of pores. We also proposed an equation to correlate the average bubble diameter with parameter of channel structure, phase ratio, and *Ca* number of continuous phase. The predicted data fit the experimental data well.

We proposed a design schematic of microsieve dispersion device, and accordingly designed a dual-size pore device based on the generation rules derived above to optimize the performance of dispersion. By adjusting the pore diameter to operating flow rate, we made activation of all pores much easier and flow rate through each pore uniform. The monodispersed bubbles can be prepared in our experiment. This work may provide guidance for scaling up and well design of the gas-liquid dispersion process qualitatively and quantitatively. Comparison with other previous works on liquid-liquid system also gives an overall understanding of microsieve devices.

Acknowledgment

The authors would like to acknowledge the support of the National Natural Science Foundation of China (U1463208, 91334201).

Literature Cited

1. Yu IF, Yu YH, Chen LY, Fan SK, Chou HYE, Yang JT. A portable microfluidic device for the rapid diagnosis of cancer metastatic potential which is programmable for temperature and CO_2. *Lab Chip*. 2014;14:3621–3628.
2. Houshmand F, Peles Y. Impact of flow dynamics on the heat transfer of bubbly flow in a microchannel. *J Heat Transfer*. 2014;136:022902.
3. Teh SY, Lin R, Hung L-H, Lee AP. Droplet microfluidics. *Lab Chip*. 2008;8:198–220.
4. Huebner A, Sharma S, Srisa-Art M, Hollfelder F, Edel JB, DeMello AJ. Microdroplets: a sea of applications? *Lab Chip*. 2008;8:1244–1254.
5. Tan J, Du L, Lu YC, Xu JH, Luo GS. Development of a gas–liquid microstructured system for oxidation of hydrogenated 2-ethyltetrahydroanthraquinone. *Chem Eng J*. 2011;171:1406–1414.
6. Tan J, Xu JH, Wang K. Rapid measurement of gas solubility in liquids using a membrane dispersion microcontactor. *Ind Eng Chem Res*. 2010;49:10040–10045.
7. Zheng C, Tan J, Wang YJ, Luo GS. CO_2 solubility in a mixture absorption system of 2-amino-2-methyl-1-propanol with ethylene glycol. *Ind Eng Chem Res*. 2013;52:12247–12252.
8. Ganan-Calvo AM, Gordillo JM. Perfectly monodisperse microbubbling by capillary flow focusing. *Phys Rev Lett*. 2001;87:274501.
9. Yasuno M, Iwamoto M, Sugiura S, Nakajima SM, Shono A, Satoh K. Monodispersed microbubble formation using microchannel technique. *AIChE J*. 2004;50:3227–3233.
10. Sobieszuk P, Aubin J, Pohorecki R. Hydrodynamics and mass transfer in gas-liquid flows in microreactors. *Chem Eng Technol*. 2012;35:1346–1358.
11. Thorsen T, Roberts RW, Arnolds FH, Quake SR. Dynamic pattern formation in a vesicle-generating microfluidic device. *Phys Rev Lett*. 2001;86:4163–4166.
12. Umbanhowar PB, Prasad V, Weitz DA. Monodisperse emulsion generation via drop break off in a coflowing stream. *Langmuir*. 2000;16:347–351.
13. Fu T, Ma Y, Funfschilling D, Zhu C, Li HZ. Breakup dynamics of slender bubbles in non-Newtonian fluids in microfluidic flowfocusing devices. *AIChE J*. 2012;58:3560–3567.
14. Dai L, Cai WF, Xin F. Numerical study on bubble formation of a gas-liquid flow in a T-junction microchannel. *Chem Eng Technol*. 2009;32:1984–1991.
15. Kobayashi I, Takano T, Maeda R, Wada Y, Uemura K, Nakajima M. Straight-through microchannel devices for generating monodisperse emulsion droplets several microns in size. *Microfluid Nanofluid*. 2008;4:167–177.
16. Nisisako T, Torii T. Microfluidic large-scale integration on a chip for mass production of monodisperse droplets and particles. *Lab Chip*. 2008;8:287–293.
17. Geerken MJ, Groenendijk MNW, Lammertink RGH, Wessling M. Micro-fabricated metal nozzle plates used for water-in-oil and oil-in-water emulsification. *J Membr Sci*. 2008;310:374–383.
18. Li SW, Xu JH, Wang YJ, Luo GS. Liquid-liquid two-phase flow in pore array microstructured devices for scaling-up of nanoparticle preparation. *AIChE J*. 2009;55:3041–3051.
19. Wang K, Lu YC, Xu JH, Luo GS. Droplet generation in micro-sieve dispersion device. *Microfluid Nanofluid*. 2011;10:1087–1095.
20. Shao HW, Lu YC, Wang K, Luo GS. Liquid–liquid flow and mass transfer characteristics in micro-sieve array device with dual-sized pores. *Chem Eng J*. 2012;193:96–101.
21. Tan J, Du L, Xu JH, Luo GS. Surfactant-free microdispersion process of gas in organic solvents in microfluidic devices. *AIChE J*. 2011;57:2647–2656.
22. Wang CY. Stokes flow through a periodically constricted tube and the resistance due to a contraction. *Acta Mech*. 2001;148:55–61.

Manuscript received Aug. 31, 2014, and revision received Feb. 5, 2015.